A dedicated small-angle X-ray scattering beamline with a superconducting wiggler source at the NSRRC

Din-Goa Liu, Chien-Hung Chang, Chin-Yen Liu, Shih-Hung Chang, Jwei-Ming Juang, Yen-Fang Song, Kuan-Li Yu, Kuei-Fen Liao, Ching-Shiang Hwang, Hok-Sum Fung, Ping-Chung Tseng, Chi-Yi Huang, Liang-Jen Huang, Shih-Chun Chung, Mau-Tsu Tang, King-Long Tsang, Yu-Shan Huang, Chien-Kuang Kuan, Yi-Chih Liu, Keng S. Liang and U-Ser Jeng*

National Synchrotron Radiation Research Center, Hsinchu 30076, Taiwan.
E-mail: usjeng@nsrrc.org.tw

At the National Synchrotron Radiation Research Center (NSRRC), which operates a 1.5 GeV storage ring, a dedicated small-angle X-ray scattering (SAXS) beamline has been installed with an in-achromat superconducting wiggler insertion device of peak magnetic field 3.1 T. The vertical beam divergence from the X-ray source is reduced significantly by a collimating mirror. Subsequently the beam is selectively monochromated by a double Si(111) crystal monochromator with high energy resolution ($\Delta E/E \simeq 2 \times 10^{-4}$) in the energy range 5–23 keV, or by a double Mo/B_4C multilayer monochromator for 10–30 times higher flux ($\sim 10^{11}$ photons s^{-1}) in the 6–15 keV range. These two monochromators are incorporated into one rotating cradle for fast exchange. The monochromated beam is focused by a toroidal mirror with 1:1 focusing for a small beam divergence and a beam size of ~ 0.9 mm $\times$ 0.3 mm (horizontal $\times$ vertical) at the focus point located 26.5 m from the radiation source. A plane mirror installed after the toroidal mirror is selectively used to deflect the beam downwards for grazing-incidence SAXS (GISAXS) from liquid surfaces. Two online beam-position monitors separated by 8 m provide an efficient feedback control for an overall beam-position stability in the 10 μm range. The beam features measured, including the flux density, energy resolution, size and divergence, are consistent with those calculated using the ray-tracing program *SHADOW*. With the deflectable beam of relatively high energy resolution and high flux, the new beamline meets the requirements for a wide range of SAXS applications, including anomalous SAXS for multiphase nanoparticles (*e.g.* semiconductor core-shell quantum dots) and GISAXS from liquid surfaces.

1. Introduction

The National Synchrotron Radiation Research Center (NSRRC) operates a third-generation synchrotron facility with a 1.5 GeV storage ring, which is based on a top-up injection mode for a constant electron beam current of 300 mA. Although the accelerator was built for VUV and soft X-ray applications, the ever-increasing hard X-ray users constantly urge for more hard X-ray sources. Recently, the success in designing and operating superconducting magnets of a few teslas at the NSRRC has greatly facilitated the development of hard X-ray sources with the low-energy

storage ring (Hwang *et al.*, 2002). Within a few years, three hard X-ray beamlines for imaging, absorption and diffraction were built with a superconducting-wavelength-shifter insertion device with a magnetic field of 5 T (Song *et al.*, 2007). Another three hard X-ray beamlines followed, for protein crystallography and membrane diffraction, using a superconducting wiggler insertion device of 3.2 T. Despite all of the straight sections of the 120 m-circumference ring being fully utilized, a specially designed in-achromat superconducting wiggler insertion device (IASW6) of compact size (0.96 m) was able to fit into the space saved from a major upgrade of the ring for a superconducting RF module system (Wang *et al.*,
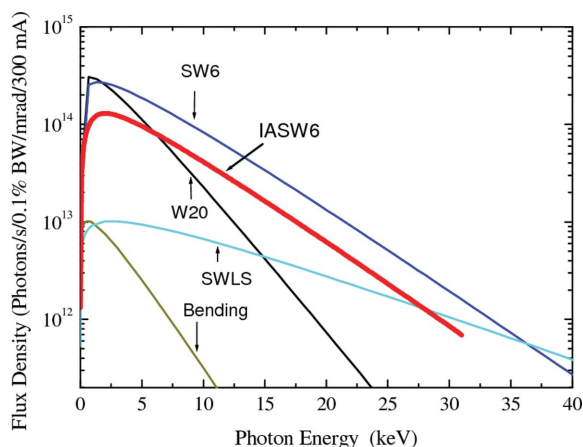
Figure 1
Comparison of the photon flux densities of the several X-ray sources at the NSRRC, including a bending magnet, the BL01 superconducting wavelength shifter (SWLS) with field strength 5.0 T, the BL17 wiggler (W20), the BL13 superconducting wiggler (SW6) with field strength 3.2 T, and the BL23 in-achromatic superconducting wiggler (IASW6) with field strength 3.1 T.

2006). With the new IASW6 hard X-ray source, we have installed a dedicated small-angle X-ray scattering (SAXS) beamline to provide a low-divergence beam of relatively high flux density and high energy resolution in the energy range 5–23 keV for nanostructural studies, as detailed below.

2. In-achromatic superconducting wiggler insertion device (IASW6)

The 16-pole IASW6 source magnet, with a period length $\lambda' = 6.1$ cm, was constructed with NbTi superconducting wires of diameter 0.64 mm. After 87 training times, a field strength of 3.1 T could be obtained at an excitation current of 265 A. The source magnet was furthermore trained 14 times after being installed on the arc section between the first and second bending magnets of the triple-bend achromat lattice storage

Table 1
Characteristics of IASW6 (with 300 mA beam current).

Number of poles	16
Magnet period, λ'	6.1 cm
Peak magnetic field, B, at 265 A	3.1 T
Deflection parameter, K ($= 0.934B\lambda'$)	17.7
Photon beam size: divergence: σ_x (σ_y);	0.37 (0.047) mm;
σ_x' (σ_y')†	0.224 (0.117) mrad
Total power	2.0 kW

† Calculated values for 15 keV photons: σ_x (σ_y): horizontal (vertical) beam size [half width at half-maximum (HWHM)]; σ_x' (σ_y'): horizontal (vertical) beam divergence (HWHM).

ring (Chang *et al.*, 2006). A magnetic gap of 19 mm was adopted to accommodate the thickened UHV beam duct used for reducing radiation from the two nearby bending magnets. Owing to the location of the arc section, the radiation source size is significantly broadened in the horizontal direction compared with the other superconducting X-ray sources at the NSRRC (Song *et al.*, 2007). Nevertheless, the IASW6 source can provide a comparable high photon flux density in the energy range 5–23 keV (Fig. 1), with the characteristic parameters summarized in Table 1.

3. Beamline design

The BL23A SAXS beamline outlined in Fig. 2 is designed for a wide range of SAXS applications (Lai *et al.*, 2006), including time-resolved SAXS, anomalous SAXS and grazing-incidence SAXS (GISAXS) from liquid surfaces. Upstream of the beamline an X-ray beam-position monitor (XBMP) was installed 4.7 m away from the X-ray source. A water-cooled aperture of 3.1 mm × 8.0 mm [horizontal (H) × vertical (V)], 6.1 m from the radiation source, gauges a radiation fan of 0.5 mrad in the horizontal direction from the IASW6. The low-energy photons (below 5 keV) of the beam are suppressed by a Be filter of thickness 600 μm to reduce the heat load of the downstream optical components. The vertical beam diver-
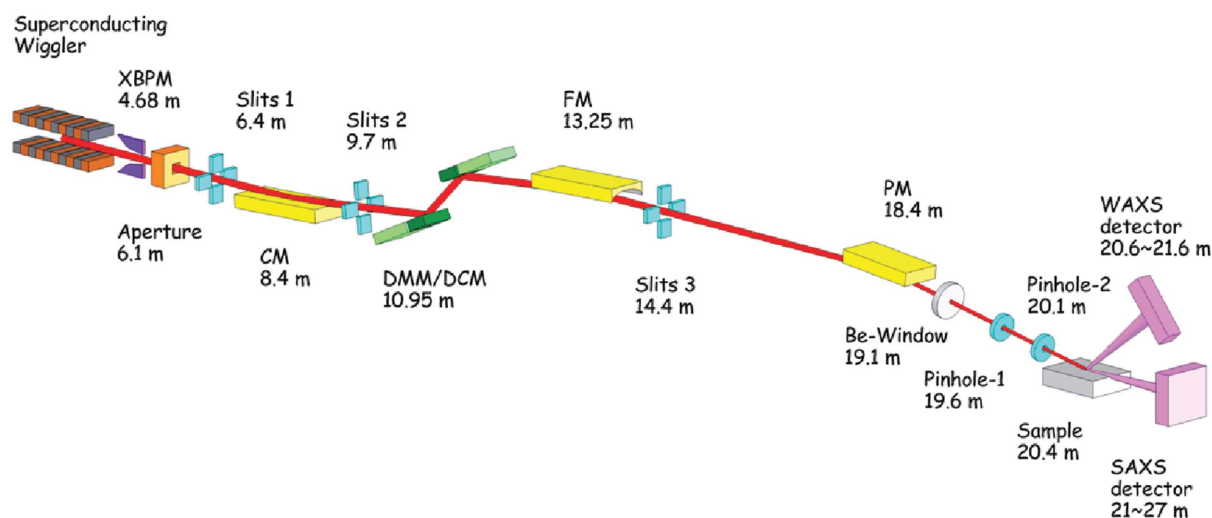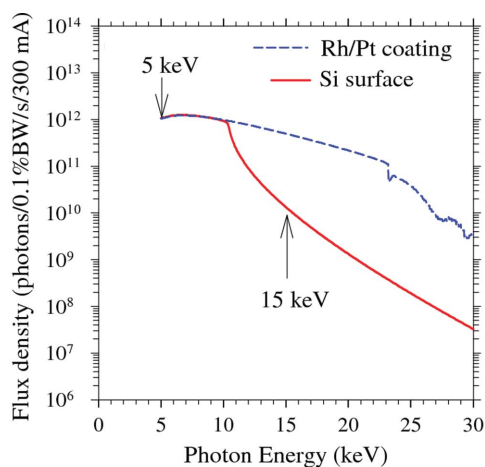

Figure 2
BL23A SAXS beamline layout, with the X-ray beam-position monitor (XBPM), collimating mirror (CM), double-crystal/multilayer monochromators (DCM/DMM), focusing mirror (FM) and plane mirror (PM). Situated in the experimental hutch are two pinhole systems and detectors for small- and wide-angle X-ray scattering (SAXS and WAXS).
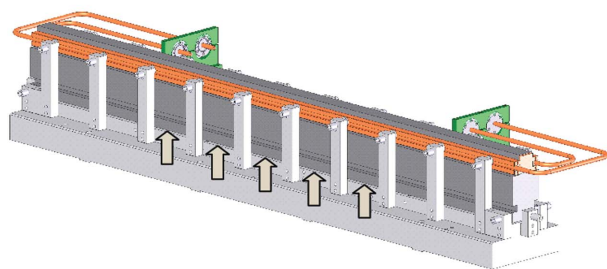
gence is reduced by a collimating mirror (CM) (at 8.4 m) placed behind the Be filter. Subsequently the beam is mono-chromated either by a double-crystal monochromator (DCM) for high energy resolution or by a double-multilayer mono-chromator (DMM) for high photon flux. The monochromated beam is then focused by a toroidal mirror (FM) with 1:1 horizontal focusing for a beam size of 0.9 mm × 0.3 mm (H × V) at the focus point 26.5 m from the radiation source. A plane mirror at 18.4 m can deflect the beam downwards for an appropriate incident angle on liquid surfaces in the GISAXS mode. In between the optical components, three sets of slits are used for beam collimation. The Be window (250 µm) located at 19.1 m separates the experimental hutch from the beamline section.

3.1. Collimating mirror

With a tangential radius of 5600 m and a sagittal radius of infinity, the 1 m-long silicon-based CM of dimensions 1000 × 55 × 100 mm [length × width × thickness (L × W × T)] can reduce the divergence of the beam from the IASW6 by a factor of ten. Half of the CM surface is coated with a Rh/Pt bilayer, consisting of an 8 nm Rh layer on top of a 25 nm Pt layer, to provide a cut-off X-ray energy of 23 keV at a 3.0 mrad beam incidence. The Rh layer can minimize the L_3- and L_2-

edge absorptions (11.564 and 13.273 keV) of the Pt layer, whereas the Pt layer provides a better reflectivity for higher-energy photons (MacDowell *et al.*, 2004). On the other hand, with the uncoated Si surface the CM has a cut-off energy at 10 keV with 3.0 mrad beam incidence, and can efficiently suppress third-harmonic photons for low-energy beams (5–10 keV). For instance, in the extreme case at 5 keV, the intensity of the third-harmonic X-rays, 15 keV, can be reduced by two orders of magnitude with the uncoated Si strip of the CM (Fig. 3a). Note that the DCM with Si(111) crystals (detailed below) gives another intensity suppression factor of two orders of magnitude ($\sim$0.4%) on high harmonic X-rays, owing mainly to the much smaller Darwin width of Si(333), 0.79″, than of Si(111), 11.5″. Five pairs of spring plungers were installed on the water-cooled CM holder (Fig. 3b) to correct the 10% manufacture slope error of the CM measured by a long trace profile.

3.2. DCM/DMM

A schematic view of the dual-monochromator system is shown in Fig. 4(a), with the DCM and DMM integrated into one rotating cradle for a fast exchange between the two monochromators of a common and constant beam exit. The DCM/DMM system resembles that used at the Advanced
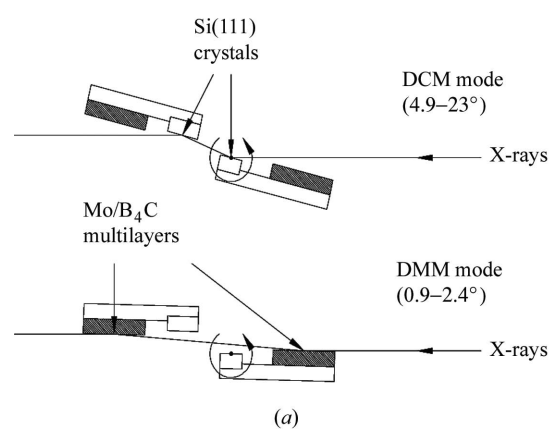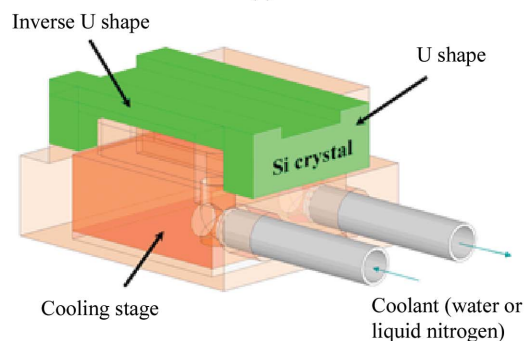
(a)

(b)

Figure 3
(a) Calculated photon flux density profiles for the beams reflected from the Rh/Pt-coated and the bare Si surfaces of the CM. The intensity dip around 23 keV for the former is due to the K-edge absorption of Rh at 23.22 keV. (b) The CM with water-cooling pipes is on a holder equipped with five spring plungers (indicated by arrows) for correcting the manufacture slope error.

(a)

(b)

Figure 4
(a) Schematic view of the DCM/DMM dual monochromators, with the rotating center of the whole system situated at the center of the first crystal. (b) With the thin central region (50 × 20 × 3 mm), the double-U (back to back) Si crystal allows the cooling block to reach closer to the irradiated crystal surface for a more uniform temperature gradient between the crystal surface and the cooling block.

Light Source (Kunz *et al.*, 2005) but differs slightly from that at the Stanford Synchrotron Radiation Laboratory (Tsuruta *et al.*, 1998). Specifically, the monochromator cradle rotates with the axis passing through the center of the first crystal (and perpendicular to the incident beam) to select an incident angle for the DCM or DMM. Starting from low incident angles, the DMM with two Mo/B_4C multilayers (2*d* spacing = 50.6 Å) first intercepts the beam at 0.9° for 15 keV X-rays and can deliver 6 keV X-rays with an incident angle of 2.4°. With further rotation of the system, the Si(111) crystals of the DCM can fully take over the incident beam at 4.9° for 23 keV X-rays, and can deliver a 5 keV beam at a maximum incident angle of 23°.

The maximum thermal loading of the first crystal of the DCM is about 6.6 W or 0.4 W mm^{-2} with a 5 keV beam when it receives 0.2 mrad irradiation from the source at a 300 mA stored electron beam current. The slope error of the crystal induced by the heat load is relaxed at higher energies owing to larger beam footprints on the crystal surface. Based on the 5 keV case of a maximum slope error, several cooling methods for the DCM were evaluated, including a direct cooling method with specially designed cooling channels arranged in an arc shape near the crystal surface (MacDowell *et al.*, 2004) and an indirect cooling with different types of flow channels. We found that a specially designed double-U shape crystal with a thin central area (50 × 20 × 3 mm, L × W × T) could be efficiently uniformly cooled by an indirect water-cooling block placed 3 mm beneath the crystal surface (Fig. 4*b*). Mechanically, the double-U shape strengthens the structure of the thin central area of the crystal. Based on a finite-element analysis (MacDowell *et al.*, 2004) with a water flow rate of 2 l min^{-1} (293 K), the double-U crystal has a thermally induced slope error that is ~30% less than that of a conventional plano crystal. Thermal insulation for liquid-nitrogen cooling has also been installed on the first crystal and first multilayer as a back-up for a higher heat load that may be encountered in a future upgrade of the storage ring for a brighter radiation source. The second crystal of the DCM, without cooling, is of a conventional plano shape.

Each of the two multilayers of the DMM (190 × 30 × 33 mm, L × W × T) consists of 200 periods of Mo/B_4C on a Si substrate (single layer thickness = 25.3 Å) for a primary Bragg reflection in the 6–15 keV range. With an energy bandwidth of ~1% and a reflectivity of 0.55, the DMM monochromated beam has a photon flux ~30 times (nominally) higher than that given by the DCM. With the available coating technique, the reflectivity from the unwanted second-order Bragg reflection of the DMM can be suppressed to less than 0.3% of the primary beam (Tsuruta *et al.*, 1998), as proved with 8 keV in-house X-rays. The first multilayer is water-cooled by the same cooling system as for the DCM, whereas no cooling is employed for the second multilayer.

3.3. Focusing mirror and plane mirror

With fixed tangential and sagittal radii of 8833 m and 39.8 mm, respectively, the toroidal focusing mirror (FM) (13.25 m from the radiation source) can focus the beam horizontally and vertically to a position 26.5 m from the source, with 1:1 horizontal demagnification. The FM, having dimensions of 1000 × 60 × 90 mm (L × W × T), is coated with the same Rh/Pt bilayer as that of the CM for the same cut-off X-ray energy of 23 keV at a 3.0 mrad beam incidence. With the FM surface facing downwards and with the same incident angle for the CM, the beam reflected from the FM is level. Our ray-tracing result using *SHADOW* (Lai & Cerrina, 1986; Padmore, 2000; Welnak *et al.*, 1994) proposes a better intensity with 2:1 horizontal focusing; nevertheless, we trade the better intensity (2:1 focusing) for a smaller beam divergence with 1:1 focusing favored in high-resolution SAXS (detailed below).

The last optical component of the beamline is the Si-based plane mirror (PM) with dimensions of 500 × 50 × 100 mm (L × W × T). Situated in a UHV chamber (18.4 m from the source) with the mirror surface facing down, the PM can deflect the beam downwards for GISAXS with liquid surfaces. For example, with an 8 keV beam of diameter 0.5 mm and an incident angle of 0.075° (corresponding to a footprint of 380 mm), the PM can deflect the beam for a typical incident angle of 0.15° onto a water surface for total reflection. With the same two-strip coating as that of the CM, the PM has the same cut-off X-ray energy of 23 keV with the 3 mrad beam incidence on the Rh/Pt-coated surface. With the uncoated Si surface, the PM can suppress high-harmonic photons for low-energy beams (5–10 keV), as in the case of the CM.

4. Performance

4.1. Beam features

With a set-up shown in Fig. 5(*a*), the measured vertical beam divergence before the CM is 0.37 ± 0.02 mrad, which is close to the 0.35 mrad calculated for an 8 keV beam using *SHADOW*. Reflected from the CM, the beam has a much smaller beam divergence of ~0.04 mrad. With the CM removed from the beam path, we have measured the changes of beam width and peak intensity as a function of the S1 slit-opening, using the second beam-position monitor BPM2 (Figs. 6*a* and 6*b*). The vertical and horizontal water-cooled BPM can scan beam profiles (Fig. 5*b*) in the respective directions. As a result, both the peak intensities and beam widths measured deviate from a linear behavior (dashed fitted lines in Figs. 6*a* and 6*b*) at a horizontal slit-opening S1$_H$ ≃ 0.6 ± 0.1 mm and a vertical slit-opening S1$_V$ ≃ 0.35 ± 0.1 mm, respectively. Based on the differences between the measured peak intensities and the linear approximation with a uniform radiation source (Figs. 6*a* and 6*b*), we have extracted an approximated radiation source size, as shown in Fig. 6(*c*). The measured horizontally extended source size, 0.85 ± 0.1 mm [full width at half-maximum (FWHM)] (Fig. 6*c*), is partially attributed to the location of the IASW6 at the arc section of the storage ring; the size is, nevertheless, consistent with the value of 0.87 mm calculated using 60 μm horizontal electron trajectory amplitude of the IASW6, $x_o = K\lambda'/(\gamma 2\pi)$ (Margaritondo, 1988), together with the spread caused by the non-zero

dispersion function at the arc section. On the other hand, the observed vertical source size, $\sim 0.45 \pm 0.1$ mm (FWHM) (Fig. 6c), is larger than the calculated value of 0.11 mm, implying a possibly skewed quadrupole magnetic field of the superconducting wiggler.
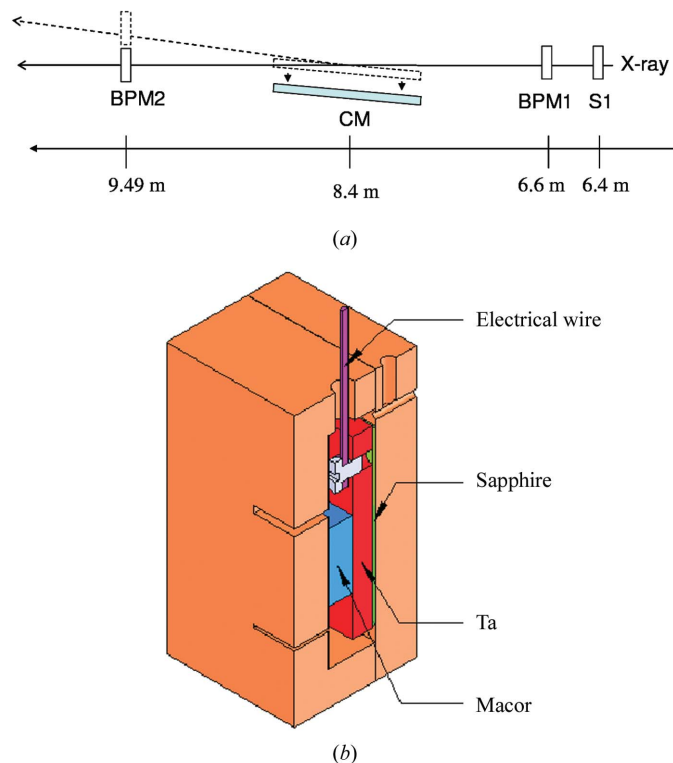

Figure 5
(a) Measurement set-up for the beam divergence and radiation source size. The first slit set S1 controls the acceptant angle of the BPMs, whereas BPM1 and BPM2 scan beam profiles at 6.6 and 9.49 m, respectively. (b) Cross-section view of the vertical or horizontal BPM, which consists of a Ta plate electrically insulated from the water-cooled copper housing by Macor spacers and a sapphire plate of good thermal conduction between the Ta plate and the copper housing. Two front slots (12×1 mm and 12×0.4 mm) separated by 15 mm can be selectively used for beam-profile scans, based on the steady photoelectrical current of the shielded Ta plate upon receiving irradiation.
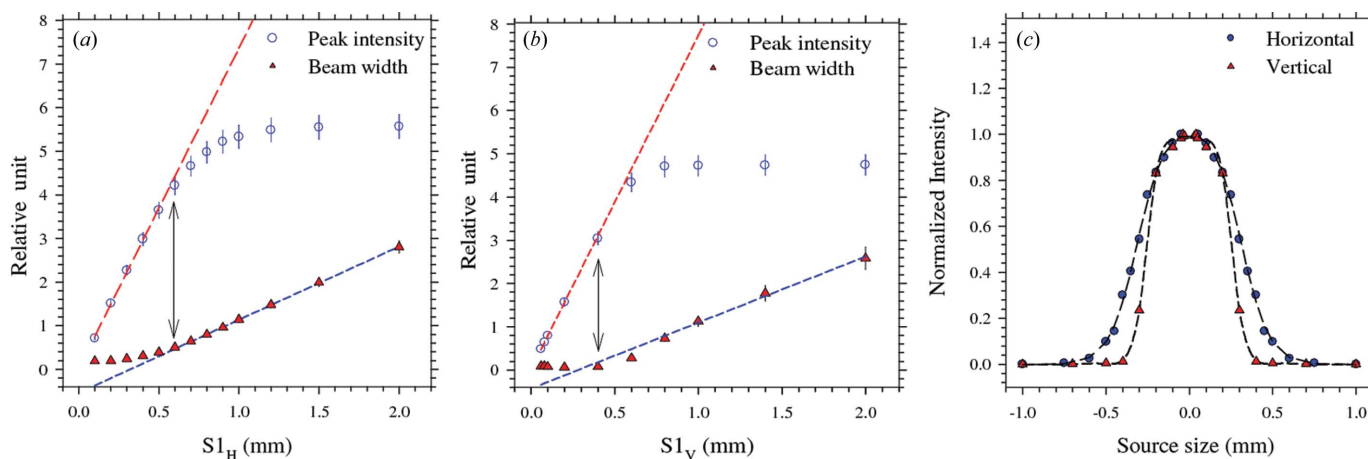
With 1:1 horizontal focusing, the slowly varying beam sizes measured with an 18 keV beam at 19.2 m (0.94×0.49 mm, H × V; FWHM), 23.0 m (0.85×0.41 mm) and the focus point 26.5 m (0.90×0.34 mm) (Fig. 7a) indicate a low beam divergence. The results are consistent with the beam sizes simulated using the ray-tracing program *SHADOW* (Fig. 7b) (Peatman, 1997; Als-Nielsen & McMorrow, 2001) over the 10 m experimental hutch (19–29 m from the radiation source). Fig. 7(b) shows the simulated beam image at the focus point, having a consistent beam size of 0.77×0.31 mm. Similar beam sizes and divergence are measured with an 8 keV beam.

4.2. Photon flux density and energy resolution

Using an ion chamber (15 cm in length) filled with 1 atm nitrogen gas, we measured the flux density $I(E) = i\varepsilon/(EAeL)$ of the DCM monochromated beam with two S1 slit-openings of 0.7×0.7 mm and 0.3×0.7 mm (H × V). Here, i is the ion chamber current (A), ε (= 35 eV) is the energy dissipation per ion pair of nitrogen gas, E is the X-ray energy, A is the X-ray absorption of nitrogen (1 atm) per cm, e is the electron charge, and L is the length of the ion chamber (Knoll, 1989). Note that the 0.7 mm opening in the vertical direction is a convenient setting to ensure a full acceptation of the beam in this direction. With the larger S1 opening, the measured photon flux densities (Fig. 8), $\sim 10^{10}$ photons s^{-1} in the energy range 5–23 keV (DCM), match in general the values calculated using *SHADOW* together with an IASW6 source spectrum generated by the *XOP* code (http://www.esrf.eu/computing/scientific/xop2.1/documentation.html). On the other hand, the flux density profile measured with the smaller S1 opening, resulting in a smaller focused beam size of 0.5×0.3 mm (H × V) for high-resolution SAXS, lies slightly below the simulated curve (Fig. 8). In the calculation, the flux losses owing to the slope errors of the DCM crystals, CM and FM have been taken into account.

By rocking the second Si crystal of the DCM, the measured energy resolutions, $\sim 2 \times 10^{-4}$, in the energy range 5–23 keV
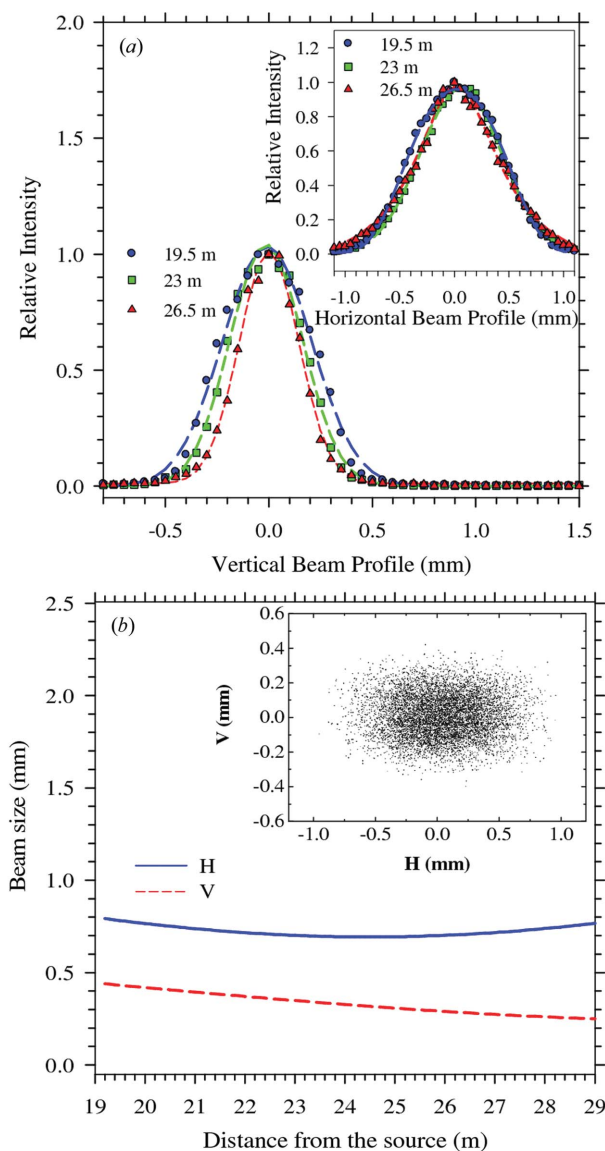

Figure 6
Peak intensities (circles) and beam widths (triangles; FWHM) of the beam profiles scanned by BPM2 as functions of the horizontal (H) and vertical (V) slit-openings $S1_H$ in (a) and $S1_V$ in (b), respectively. Both sets of data deviate from the uniform radiation approximation (dashed fitted lines) at $S1_H \simeq 0.6$ mm (H) and $S1_V \simeq 0.35$ mm (V). Shown in (c) is the approximated radiation source profiles in the vertical and horizontal directions.

Figure 7
(a) Vertical and horizontal (inset) beam profiles of an 18 keV beam measured at 19.2, 23 and 26.5 m. (b) Simulated beam size over the 10 m experimental hutch (19–29 m from the radiation source). The inset shows the simulated beam image at the focus point, 26.5 m.

Figure 8
Flux densities of the DCM monochromated beams measured at 19.2 m (near the designated SAXS sample position) with two S1 slit-openings of 0.3×0.7 mm (H $\times$ V) (solid circles) and 0.7×0.7 mm (solid squares). The data are compared with the simulation curves (long- and short-dashed curves). Also shown is the flux density profile of the BL17B3 SAXS beamline of the NSRRC (empty circles) at a stored beam current of 300 mA. The inset shows the measured and simulated (dashed curve) energy resolutions with the larger S1 opening on an absolute scale of eV and a relative scale of $\Delta E/E$, respectively.

shown in Fig. 9(b). After the calibration, the DCM can robustly define the absolute beam energy in the range 5–23 keV with an accuracy better than 6 eV (inset of Fig. 9b).

With the same measurement geometry as with the DCM, the photon flux densities measured with the DMM monochromated beam (S1 slits = 0.3×0.7 mm, H $\times$ V) are 10–30 times higher than those measured with the DCM in the energy range 6–15 keV (Fig. 10). The corresponding energy resolution is $\sim 1.1 \times 10^{-2}$ in general (inset of Fig. 10). The overall performance of the DMM is comparable with that reported by Tsuruta *et al.* (1998) or Kunz *et al.* (2005). Table 2 summarizes the characteristics of the DCM and DMM.

4.3. Beam-position stability

We have utilized the four stable blade currents (of the order of tens to hundreds of pico-amperes) of the third slit set S3 (14.1 m from the source), when subject to irradiation, as an online beam-position monitor. The beam positions in the vertical and horizontal directions are calibrated to an accuracy of a few micrometers using the summations and differences of the blade currents of the top–bottom and right–left blade pairs, respectively. This beam-position monitor together with the XBPM (monitoring the vertical beam position), separated by ~ 8 m, provide an online feedback control for an overall beam-position stability in the 10 µm range. On the other hand, the beam-position shifts near the designated sample position (19.2 m from the source) during a change of beam energy *via* DCM (5–23 keV) or DMM (6–15 keV) are less than 50 µm in

(inset of Fig. 8) fall closely on the calculated curve; the calculation takes into account the vertical beam divergence, the Darwin width and the heat-load-induced slope error of the Si(111) crystals of the DCM, and the slope errors of the CM and FM. The result implies that the specially designed double-U shape crystal may duly suppress the heat-load-induced slope error. We have used X-ray absorption near-edge spectroscopy (XANES) to calibrate the absolute beam energy. Fig. 9 illustrates an example with a standard Cu foil of the K-edge absorption at 8979 eV. The energy resolution of 2.0 eV derived from the XANES result (inset of Fig. 9) matches well with that (2.1 eV) measured using the rocking-crystal method (Fig. 8). Using 14 standard metal foils with characteristic X-ray absorption edges covering 5–23 keV, we have calibrated the beam energy defined by the DCM in a systematic way, as
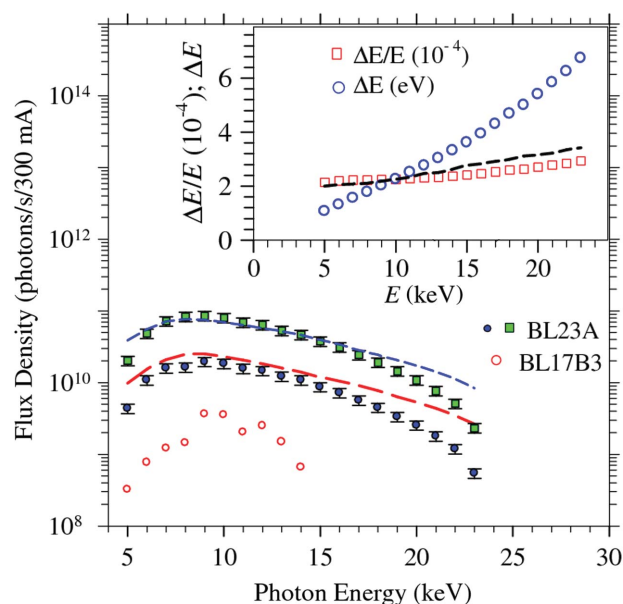
both the vertical and horizontal directions, as shown in Fig. 11(*a*). The beam position shift owing to the switch from the DCM to the DMM at a constant beam energy is less than 30 µm in the vertical direction (Fig. 11*b*), whereas the constant shift of ~60 µm in the horizontal direction (Fig. 8), reflecting a non-ideal alignment between the crystals and multilayers, can be easily corrected by an offset after each DCM/DMM switch.

Table 2
Characteristics of the DCM and DMM.

	Crystal type	Dimensions (mm)	E (keV)	$\Delta E/E$	θ (°)†	Flux (photons s⁻¹)‡
DCM	Si(111)	1st: 50 × 20 × 3§ 2nd: 50 × 40 × 40	5–23	2–5 × 10⁻⁴	4.9–23	10⁹–10¹⁰
DMM	Mo/B₄C	190 × 30 × 33	6–15	1.1 × 10⁻²	0.9–2.4	1–4 × 10¹¹

† Incident angle.   ‡ Measured with the S1 opening = 0.3 × 0.7 mm (H × V).   § Dimensions of the central area of the double-U shape crystal. The full dimensions of the first crystal are 70 × 40 × 40 mm (L × W × T).

5. Features of the SAXS end-station

With the new X-ray beamline, the SWAXS (small- and wide-angle X-ray scattering) instrument previously installed at the
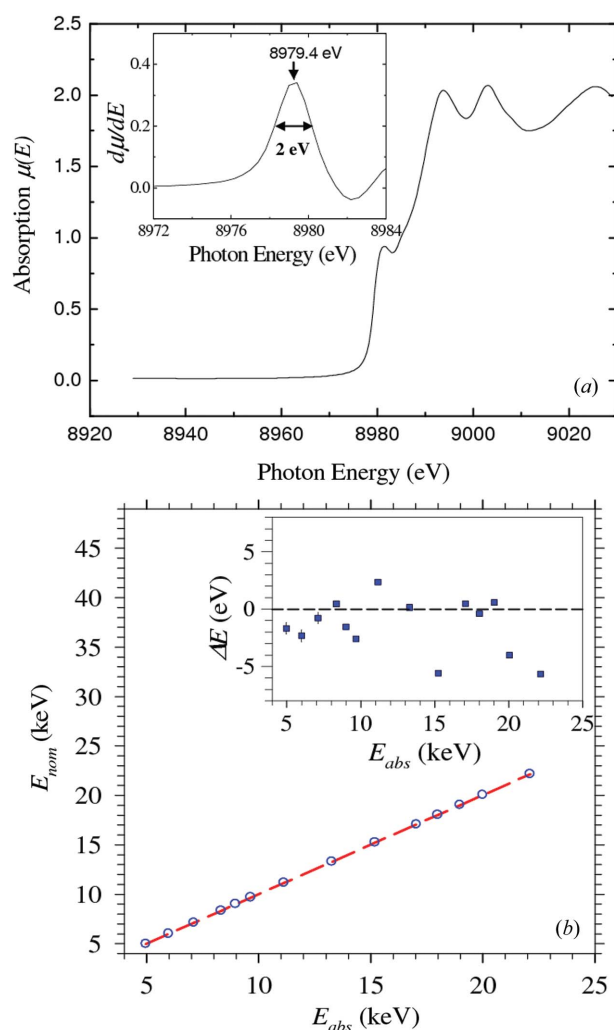

Figure 9
(*a*) XANES of a Cu foil measured with the DCM monochromated beam. The inset shows the derivative profile of the XANES spectrum, with the peak position corresponding to the Cu *K*-edge absorption at 8979 eV and the peak width 2.0 eV representing the energy resolution of the beam. (*b*) The DCM defined energies (nominal energy E_{nom}) are calibrated by the characteristic absorption edges (absolute energy E_{abs}) of 14 standard metal foils measured using XANES. From the fitted line, an energy-dependent shift of 0.2% and a common offset of 11 eV of E_{nom} are corrected systematically. The inset shows the deviations of E_{nom} from E_{abs} after the corrections.

BL17B3 end-station will be relocated to the new BL23A end-station of a 10 × 4 m (L × W) experimental area. The SWAXS instrument, detailed in a previous study (Lai *et al.*, 2006), is equipped with an area detector for SAXS (a gas-type linear proportional counter) and a linear detector (gas-type) for WAXS, for which two detectors are connected to two data acquisition systems operated in a master–slave mode. Such an instrument configuration is suitable for time-resolved simultaneous SAXS and WAXS.

For high-resolution SAXS, it is important to have not only a small beam size but also a small beam divergence. For instance, using an 8 keV beam of diameter 0.5 mm and beam divergence of 0.2 mrad coupled with a sample-to-detector distance of 5 m, a beamstop of diameter 4 mm and a detector pixel size of 200 µm, we can have a *Q*-resolution of ~20% of the minimum *Q* value of 0.002 Å⁻¹, which corresponds to a measurable lamellar spacing of 300 ± 60 nm. Here, $Q = 4\pi\sin(\theta)/\lambda$ is the wavevector transfer of X-rays defined by the wavelength λ and the scattering angle 2θ. For time-resolved experiments with 100 ms resolution, the DMM can provide ~10¹¹ photon s⁻¹ for a typical polymer sample (for instance, polyethylene) of 10⁻⁴ scattering efficiency, leading to ~10⁶

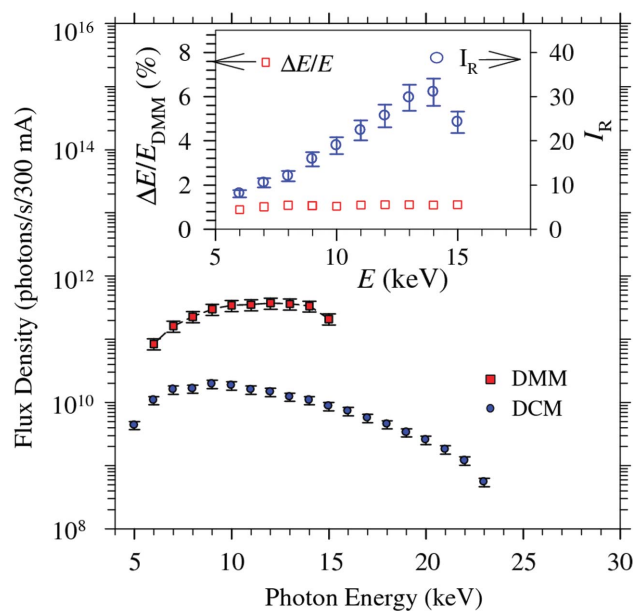**Figure 10**
The flux density profile measured with the DMM is compared with that measured with the DCM at the same S1 opening of 0.3 × 0.7 mm (H × V). The inset shows the energy resolution and the flux gain I_R (relative to that of the DCM) of the DMM monochromated beam.
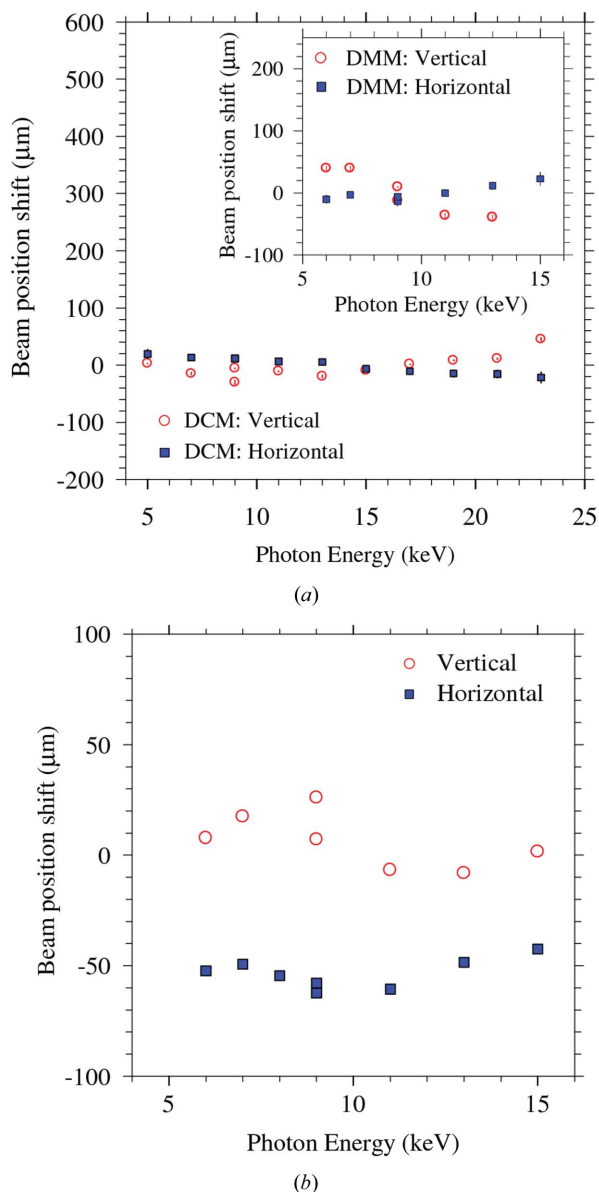
Figure 11
(*a*) Vertical and horizontal beam-position shifts measured near the designated SAXS sample position upon the changes of beam energy *via* the DCM or DMM (inset). (*b*) Beam-position shifts in the vertical and horizontal directions owing to the change of monochromator from the DCM to the DMM at a constant beam energy.

scattered photons in each data frame of a 100 ms data collection time. For anomalous SAXS, the DCM offers a resolution of several eV in the energy range 5–23 keV, covering *K*-edge or *L*-edge absorption of the atoms of atomic number higher than 23 of vanadium, with the exceptions of the atoms of atomic numbers between 45 (Rh) and 54 (Xe). For GISAXS with liquid surfaces, the PM can deflect the beam downwards for a suitable incident angle of 0.1–0.2°, depending on the interested surfaces and beam energy used.

6. Concluding remarks

With the compact in-achromat superconducting wiggler insertion device, we have installed a small-angle X-ray scattering beamline to provide a low-divergence beam of 10^{10}–10^{11} photons s^{-1} in the energy range 5–23 keV for nano-structural research. Two online beam-position monitors are used for an efficient feedback control of the beam position. Equipped with the PM and the dual DCM/DMM monochromators for a deflectable beam with relatively high energy resolution and high flux, the new SAXS beamline meets the requirements of a wide range of SAXS applications, including anomalous SAXS with multiphase nanoparticles and GISAXS with liquid surfaces. It is proved that, based on the superconducting RF module system and the superconducting source magnet, it is possible to have a SAXS beamline of reasonable performance with a small 1.5 GeV storage ring.

References

Als-Nielsen, J. & Mcmorrow, D. (2001). *Elements of Modern X-ray Physics*, ch. 2, p. 43. New York: John Wiley.
Chang, C. H., Hwang, C. S., Chen, H. H., Lin, F. Y., Huang, M. H., Fan, T. C., Jan, J. C., Chang, C. C., Hsu, S. N., Hsiung, G. Y. & Chen, J. R. (2006). *IEEE Trans. Appl. Supercond.* **16**, 1862.
Hwang, C. S., Wang, B., Wahrer, R., Chen, H. H., Lin, F. Y., Fan, T. C. & Chen, C. T. (2002). *IEEE Trans. Appl. Supercond.* **12**, 686–690.
Knoll, G. F. (1989). *Radiation Detection and Measurement*, p. 132. New York: John Wiley.
Kunz, M. *et al.* (2005). *J. Synchrotron Rad.* **12**, 650–658.
Lai, B. & Cerrina, F. (1986). *Nucl. Instrum. Methods Phys. Res. A*, **246**, 337–341.
Lai, Y.-H., Sun, Y.-S., Jeng, U.-S., Lin, J.-M., Lin, T.-L., Sheu, H.-S., Chuang, W.-T., Huang, Y.-S., Hsu, C.-H., Lee, M.-T., Lee, H.-Y., Liang, K. S., Gabriel, A. & Koch, M. H. J. (2006). *J. Appl. Cryst.* **39**, 871–877.
MacDowell, A. A. *et al.* (2004). *J. Synchrotron Rad.* **11**, 447–455.
Margaritondo, G. (1988). *Introduction to Synchrotron Radiation*, ch. 2, p. 19. Oxford University Press.
Padmore, H. A. (2000). *Advanced Light Source Notes LSBL-542*. Advanced Light Source, Berkeley, CA, USA.
Peatman, W. B. (1997). *Gratings, Mirrors and Slits: Beamline Design for Soft X-ray Synchrotron Radiation Sources*, ch. 2, p. 38. Singapore: Gordon and Breach.
Song, Y.-F. *et al.* (2007). *J. Synchrotron Rad.* **14**, 320–325.
Tsuruta, H., Brennan, S., Rek, Z. U., Irving, T. C., Tompkins, W. H. & Hodgson, K. O. (1998). *J. Appl. Cryst.* **31**, 672–682.
Wang, C., Chang, L. H., Yeh, M. S., Lin, M. C., Chung, F. T., Chang, S. S., Yang, T. T. & Tsai, M. H. (2006). *Physica C*, **441**, 277.
Welnak, C., Chen, G. C. & Cerrina, F. (1994). *Nucl. Instrum. Methods Phys. Res. A*, **347**, 344–347.